LA-UR-

Approved for public release;
distribution is unlimited.

Title: | Diffraction and coherence in breast ultrasound tomography: A study with a toroidal array

Author(s): | Francesco Simonetti, Imperial College, London, UK
Lianjie Huang, EES-11
Neb Duric and Petter Littrup, Karmanos Cancer Institute

Intended for: | Medical Physics

Los Alamos
NATIONAL LABORATORY
—— EST.1943 ——

Diffraction and coherence in breast ultrasound tomography: A study with a toroidal array

F. Simonetti*

Department of Mechanical Engineering,

Imperial College, London SW7 2AZ, UK, and

MS D443, Los Alamos National Laboratory, Los Alamos, NM 87545, USA

L. Huang

MS D443, Los Alamos National Laboratory, Los Alamos, NM 87545, USA

N. Duric and P. Littrup

Karmanos Cancer Institute, Wayne State University,

4100 John R, Detroit, Michigan 48201, USA

(Dated: 18 June 2008)

Abstract

Ultrasound is commonly used as an adjunct to mammography for diagnostic evaluation of suspicions arising from breast cancer screening. As an alternative to conventional sonography that uses hand-held transducers, toroidal array probes that encircle the breast immersed in a water bath have been investigated for ultrasound tomography. In this paper, two sets of experiments performed with a prototype ultrasound scanner on a phantom and a human breast *in vivo* are used to investigate the effects of diffraction and coherence in ultrasound tomography. Reconstructions obtained with transmission diffraction tomography (TDT) are compared with conventional reflection imaging and computerized ultrasound tomography showing a substantial improvement. The *in vivo* tests demonstrate that TDT can image the complex boundary of a cancer mass and suggest that it can reveal the anatomy of milk ducts and Cooper's ligaments.

---

*Electronic address: f.simonetti@imperial.ac.uk

I. INTRODUCTION

Since the 1970s, researchers have been exploring the potential of ultrasound tomography for the detection of breast cancer[1-3]. Indeed, ultrasound could be a very attractive alternative to the gold standard of X-ray mammography since it is intrinsically safer, it can detect some cancers that are invisible on mammograms and could lead to earlier diagnosis[4]. In addition, ultrasound technology is inexpensive compared to X-ray or MRI, thus offering the potential for the development of a dense network of screening centers that could deliver diagnostic capabilities to the bulk of the population.

While the ray model of geometrical optics is in general sufficient to describe the propagation of high energy photons in X-ray tomography of soft media; diffraction, refraction and scattering can become dominant when imaging complex objects, such as the human breast, with ultrasound. Although the anatomy of the breast is not yet completely understood[5], it is largely accepted that the gross anatomy consists of a fatty tissue and a glandular component which is arranged in lobes that are held together by a fibrous framework called Cooper's ligaments. The lobes contain lobules that are connected to the nipple by an entangled network of ducts which Cooper, in the celebrated *On the anatomy of the breast*[6], compared to the intertwined root of a tree. These structures along with lymphatic and blood vessels result in the very complex anatomy of the breast. When an ultrasonic wave travels through breast tissue, the mechanical properties of these structures produce a rich spectrum of phenomena that change the characteristics of the ultrasound field. The extent of these changes depends on the characteristic size of these structures relative to the wavelength, λ, of the probing wave. As an example, randomly distributed features on the scale of λ can result in complex interference patterns that cause the granular appearance of conventional sonograms known as speckle and which do not bear any obvious relationship to the actual anatomy[7]. Similarly, multiply scattered sound between strong, closely spaced and randomly distributed features can cause the ballistic wave transmitted through a complex medium to be followed by a complex coda statistically described by diffusion equations[8,9].

Recent progress in solid state electronics and increased computational power have reinvigorated interest in ultrasound tomography of the breast and much effort is now being devoted to the development of a new generation of ultrasound scanners that employ a toroidal array of sensors[10-13] as depicted in the diagram of Fig. 1(a). While in the early work by Carson et

al.[3] the breast was probed by means of a pair of transducers mechanically scanned around a circular aperture that encircled the breast, the toroidal array replaces the mechanical scanning with a much faster electronic switching that allows the breast to be insonified from any direction in the plane of the aperture and the scattered field to be measured all around the breast in less than 0.1 sec. Note that the speed at which the measurements are performed is crucial to avoid artifacts caused by tissue motion.

This full view configuration can be used to perform transmission measurements through the breast in conjunction with the more conventional backscattering measurements obtained with linear array probes. The combination of backscattering and transmission measurements can then be used to extract accurate information about the speed of sound and attenuation distributions within the breast. Backscattering measurements are used to reproduce compound beamforming[3] synthetically and lead to the so-called reflection image (RI). A subset of the array sensors is used to create a virtual aperture that produces different images of the breast, which are then combined together as the aperture revolves around the breast[13]. On the other hand, transmission measurements are used in computerized ultrasound tomography (CUT) to estimate the arrival time of the ballistic transmission through the breast that is subsequently used to reconstruct the speed of sound map via the Radon transform[14]. Promising results for human breast *in vivo* have been reported by Carson et al.[3] and more recently by Duric et al.[13] with a toroidal array. However, CUT is based on the ray approximation that is known to cause resolution degradation and image artifacts due to its inability to account for diffraction[15]. Therefore, it can be expected that more accurate reconstruction methods like diffraction tomography[16](DT) could lead to improved resolution. An improvement on image resolution is desirable since it would decrease the size of the minimum detectable lesion and increase the specificity of CUT by providing additional anatomical information.

The aim of this paper is to investigate the role of diffraction and coherence in ultrasound breast tomography by means of two sets of experiments performed on a phantom and a human breast in vivo. The study on the effects of diffraction employs the DT approach introduced in Ref.[17] and has a twofold objective. Fist, it is to assess if transmission diffraction tomography (TDT) leads to higher image resolution than CUT. Second, it is to investigate if RI and TDT contain complementary information. In fact, it is known that RI and CUT images complement each other since the former provides information about the boundaries

3

of regions of sudden impedance variations within the object, whereas, the latter supplies quantitative information about the spatial impedance variations[3].

While CUT requires the use of wideband (WB) insonification to time the journey of ultrasound through the breast, RI and DT can also be performed with continuous wave (CW) excitation. This is because both RI and DT can be seen as interferometric techniques that exploit spatial interference caused by waves transmitted and detected by transducers at different spatial locations. A CW image is coherent and can contain speckle. Here the coherent and incoherent superposition of different CW images, within the bandwidth of a WB insonification, is studied so as to assess the effect of frequency diversity on image noise and speckle contrast.

II.   METHODS

We conduct ultrasound tomography experiments on a phantom and a human breast *in vivo* to investigate the effects of diffraction and coherence in breast tomography. While the knowledge of the true *in vivo* anatomy is always uncertain, the properties of a phantom can be characterized accurately during its manufacturing or by means of imaging techniques that cannot be used *in vivo*, such as x-ray CT. The knowledge about the true structure of the phantom can then be used to benchmark different ultrasound imaging methods. However, *in vivo* validation of observations carried out on a phantom is paramount due to the complex biology of the actual breast.

In this paper, imaging methods based on different physical models are applied to the two experimental data sets, and the resulting reconstructions are compared against each other.

A.   Physical model

The objective of ultrasound tomography is to reconstruct the spatial distribution of a target material property from the perturbation induced by the object's structure on the free propagation of ultrasound. Such a material property is described by the object function that is related to the index of refraction map, $n(\mathbf{r})$, via the relationship $O(\mathbf{r}) = k^2[n(\mathbf{r})^2 - 1]$ where k is the wavenumber of the probing wave in the free space. For DT, central to the reconstruction is the existence of a one-to-one mapping between the perturbation, p, and

4

the spatial Fourier transform of the object function, O, which defines the so-called K-space,

$$p \longleftrightarrow O. \tag{1}$$

The definition of the perturbation in eq. (1) depends on the model used to describe the interaction between the incident wave and the probed object.

To illustrate this, let us consider the two-dimensional scattering problem depicted in Fig. 1(a) whereby a monochromatic (CW) plane wave propagating in the direction $\hat{\mathbf{r}}_0$ is incident on an object of support D. Assuming that the scattering problem can be expressed by a scalar potential, the field detected by an array sensor placed in the far field at position $\mathbf{r}$, $\psi(\mathbf{r}, k\hat{\mathbf{r}}_0)$, is given by

$$\lim_{r \to \infty} \psi(\mathbf{r}, k\hat{\mathbf{r}}_0) = \exp\left(ik\hat{\mathbf{r}}_0 \cdot \mathbf{r}\right) + f(k\hat{\mathbf{r}}, k\hat{\mathbf{r}}_0)\frac{\exp\left(ikr\right)}{\sqrt{r}}, \tag{2}$$

where the first term of the right hand side is the incident plane wave, which propagates with wavelength λ $(k = 2\pi/\lambda)$ and $f(k\hat{\mathbf{r}}, k\hat{\mathbf{r}}_0)$ is the scattering amplitude defined as

$$f(k\hat{\mathbf{r}}, k\hat{\mathbf{r}}_0) = \Pi \int_D d^2r' \exp(-ik\hat{\mathbf{r}} \cdot \mathbf{r}')O(\mathbf{r}')\psi(\mathbf{r}', k\hat{\mathbf{r}}_0), \tag{3}$$

with

$$\Pi = \frac{\exp(i\pi/4)}{\sqrt{8\pi k}}. \tag{4}$$

It can be shown that under the Born approximation, the perturbation p in eq. (1) coincides with the scattering amplitude[18]

$$p(k\hat{\mathbf{r}}, k\hat{\mathbf{r}}_0) = f(k\hat{\mathbf{r}}, k\hat{\mathbf{r}}_0) = \Pi O[k(\hat{\mathbf{r}} - \hat{\mathbf{r}}_0)]. \tag{5}$$

This relationship links the measurements to the Fourier transform of the object function, $O(\Omega)$, directly. In fact, the scattering amplitude can be measured experimentally with a toroidal array of transreceivers, by transmitting with each sensor sequentially and detecting the field with all the sensors in parallel.

Equation (5) is the physical model used in this paper to describe the interaction of the probing wave with the object. The diagram in Fig. 1 shows how a particular transmit and receive pair maps onto a point of the K-space. In particular, for a given transmitter position defined by $\hat{\mathbf{r}}_0$ the measurements map onto the circle Γ_1 as the receiver direction, $\hat{\mathbf{r}}$, spans the entire array. This is known as the Ewald circle. The solid part of the circle corresponds to the transmission measurements (the angle between $\hat{\mathbf{r}}$ and $\hat{\mathbf{r}}_0$ is less than $\pi/2$) whereas,

the dashed part corresponds to the backscattering measurements. As the position of the transmitter revolves around the object, the Ewald circle sweeps a disk of the K-space with radius $2k$ known as the Ewald Limiting Disk (ELD) and labeled as Γ_2 in Fig. 1(b).

B. Imaging methods

From the knowledge of $O(\Omega)$ within the ELD, $O(\mathbf{r})$ can be reconstructed by assuming that $O(\Omega)$ vanishes outside the ELD and performing the inverse Fourier transform. This leads to a low-pass filtered image of the object function, I_{DT}, which in the K-space is given by

$$I_{DT}(\Omega) = O(\Omega)H_{DT}(\Omega), \tag{6}$$

with

$$H_{DT}(\Omega) = \begin{cases} 1 & |\Omega| < 2k \\ 0 & |\Omega| > 2k. \end{cases} \tag{7}$$

This implies that only the characteristics of the object that vary on a spatial scale longer than $\lambda/2$ can be reconstructed, leading to the classical diffraction limit[19].

In transmission diffraction tomography (TDT), the object function is reconstructed from only the transmission measurements. Therefore, as the transmitter revolves around the object, the half solid circle in Fig. 1(b) describes a disk of radius $\sqrt{2}k$ centered at the origin and contained within the ELD. In other words, TDT provides a low-pass filtered image with cutoff $\sqrt{2}k$ rather than $2k$. A similar argument shows that reflection diffraction tomography (RDT) provides a band-pass filtered image of the object with cutoffs at $\sqrt{2}k$ and $2k$. This analysis suggests that RDT complements TDT by reconstructing the spatial frequencies between $\sqrt{2}k$ and $2k$.

RDT and TDT can be related to reflection imaging (RI) and computerized ultrasound tomography (CUT), respectively. RI can be seen as a beamforming process that provides an image of the object by focusing and steering a beam across the object. As shown in Ref.[20], the beamforming image is a filtered version of the DT reconstruction. The filter introduces a distortion of the DT image by attenuating the spatial frequencies in the order of k and amplifying those approaching $2k$.

CUT can be considered as a the limit of TDT obtained when the wavelength vanishes. This asymptotic condition is achieved in practice when the wavelength is much smaller

than the spatial scale over which variations of the object function occur, leading to the approximation of geometrical optics. In this case, k approaches to infinity and the half circle in the K-space representing the transmission measurements, Fig. 1(b), tends to a straight line passing through the origin, leading to the Fourier slice theorem[16].

C. Frequency diversity

The previous analysis has considered CW excitation only; therefore, it refers to the perfectly coherent case. It can be observed that the imaging process is the convolution of the object function with the point spread function (PSF), h,

$$I(\mathbf{r},\omega) = \int_D d^2r' h(\mathbf{r}-\mathbf{r}',\omega) O(\mathbf{r}'), \qquad (8)$$

where the PSF is the image of a point as seen by a particular imaging method and it is a function of frequency. As an example, in the case of DT, the PSF is the inverse Fourier transform of eq. (7) i. e.

$$h_{DT}(\mathbf{r},\mathbf{r}') = k\frac{J_1(2k|\mathbf{r}-\mathbf{r}'|)}{\pi|\mathbf{r}-\mathbf{r}'|}, \qquad (9)$$

where J_1 is the order one bessel function of the first kind. Figure 2 shows the modulus of the PSF as a function of the distance between a point in the object $\mathbf{r}'$ and a point in the image $\mathbf{r}$ relative to λ. The presence of a main central lobe means that only the points of the object contained within the main lobe give a significant contribution to the integral in eq. (8). Therefore, the image in $\mathbf{r}$ is given by the coherent superposition of $O(\mathbf{r}')$ within the main lobe of the PSF. If $O(\mathbf{r}')$ varies randomly within the main lobe, then the integral in eq. (8) is a random function of $\mathbf{r}$. Moreover, at a single position $\mathbf{r}$, the image does not relate to the object function at a particular point in space. These are the main implications of coherence and explain the speckle phenomenon.

In optics it is known that speckle can be suppressed by reducing the temporal coherence of the illumination[21] and thus a WB source rather than a monochromatic one should be used. In fact, optical detectors average the intensity of light over a time interval that is much longer than the characteristic period of light wavepackets. This means that in optics a WB image is given by the incoherent superposition of all the monochromatic images, $I(\mathbf{r},\omega)$, that could be reconstructed if it was possible to separate the different frequency components

of the illumination

$$I_{incho}(\mathbf{r}) = \int_{-\infty}^{\infty} d\omega |I(\mathbf{r},\omega)|^2. \tag{10}$$

Note that the superposition is incoherent because the phase information of each monochromatic image is not included in (10). On the other hand, ultrasonic sensors generate an almost instantaneous measurement of the wave field, thus allowing the harmonics contained in the insonification to be separated. As a result, RI with WB excitation is still a coherent process. In fact, the wideband version of eq. (8) becomes

$$I_{WB}(\mathbf{r}) = \left| \int_{-\infty}^{\infty} d\omega I(\mathbf{r},\omega) \right|^2, \tag{11}$$

where different monochromatic images are added coherently. The same argument applies to TDT and RDT. Moreover, for this reason speckle is present in sonography despite the fact that the insonification is not temporally coherent.

From eq. (8) it is clear that the speckle phenomenon would not occur if the imaging system were ideal, i. e. if the PSF was a delta function. In this case the image would reproduce the object function exactly. The fact that the PSF is not a delta function is due to the diffraction phenomenon that is the result of interference. This observation explains why CUT is speckle free. The assumption that $\lambda \to 0$ implies that diffraction effects are not present and that the PSF is a delta function. In other words, the ray approximation neglects interference that is the very cause for speckle and leads to its total suppression.

Finally it is important to observe that WB DT takes advantage of the entire structure of the wavepackets contained in the time traces recorded by the array for each transmit-receive pair. Each time trace is analyzed in the frequency domain and, at each frequency, the complex number that defines the Fourier transform, at that frequency, is used to produce a CW image. CW images obtained over the bandwidth of the signal are subsequently combined together to produce the final WB DT image. Therefore, if one considers a single time trace, a WB DT image depends on all the complex numbers associated with the Fourier transform of the signal and hence on all the points of the time trace. On the other hand, for a single transmit-receive pair, CUT uses one real number only that is the delay in the arrival time of the transmitted signal through the specimen relative to the propagation in a background medium. The delay is estimated from particular features of the transmitted wavepacket such as the first zero crossing point or maximum point of the signal envelope. The underlying

8

assumptions are that the wavepacket is rigidly shifted in time by the presence of the object and its amplitude decreased by attenuation while its shape is preserved. Clearly distortion of the wavepacket caused by complex structures within the breast can cause errors in the estimation of the arrival time and result in image artifacts. On the other hand, DT takes advantage of the distortion of the wavepackets to improve image resolution.

D. Experimental setup

The experiments are performed with a prototype ultrasound scanner developed at Karmanos Cancer Institute[13]. The scanner employs a toroidal array with 256 transducers mounted on a circular ring with an internal diameter of 200 mm as shown in Fig. 3(a). The array is immersed in water bath that provides the acoustic coupling between the array and the object to be imaged. The center frequency of the transducers is 1.3 MHz with ~100% bandwith, further details can be found in Ref.[13,22].

The theory above has considered the case of 2-D objects that can be reconstructed from measurements performed with a toroidal array. Although the extension of the theory to the 3-D case is trivial, limitations in current ultrasound technology, pose fundamental constraints on its practical implementation. In simple terms, while in the 2-D case it is sufficient to measure the field with sensors deployed along a circular aperture, in 3-D the presence of an additional spatial dimension requires an additional degree of freedom in the measurements. Therefore, the ultrasound field needs to be sampled over a sphere that surrounds the object rather than on a circle. However, in order to avoid aliasing effects, it is necessary to populate the sphere with a number of transducers that approximates the square of the number required in 2-D. Even though this condition can be somehow relaxed, the overall number of sensors that one would need is beyond the capabilities of current technology (for a more detailed discussion see Ref.[17]). To overcome this problem we have introduced a multi-scale approach that decouples the information contained in the 2-D plane identified by the circular aperture of the array from the global 3-D structure of the object, thus allowing a single slice of a 3-D object to be reconstructed with a circular aperture[17,20]. In this case the sampling requirements are dictated by the wavelength of the incident field and the characteristic size, l, of the object being probed. In Ref.[17] it has been shown that the minimum number of

spatial sampling points, N, required to avoid aliasing has to satisfy the inequality

$$N > 2\pi l / \lambda. \tag{12}$$

As an example, for an array with $N = 256$ and $\lambda = 2$ mm the maximum object diameter that can be imaged is $\sim$80 mm. For larger objects or shorter wavelengths, aliasing occurs and consequently, it produces grating lobes that interfere with the reconstruction and cause image artifacts.

E. Phantom

The phantom, as shown in the photograph of Fig. 3(a), consists of several materials mimicking a subcutaneous fat layer that embeds an irregular glandular region containing four different, 3-D inclusions corresponding to two tumors and two fat spheres. The glandular region contains fine powders used to reproduce the speckle effect. A X-ray CT image of a coronal slice of the phantom is displayed in Fig. 3(b), further details can be found in Ref.[13]. The phantom was immersed in the water bath at 24.0°C.

F. Human breast

In order to perform *in vivo* testing, a patient was positioned on a bed with the breast suspended in the water bath through an aperture in the bed as described in Ref.[13]. The study involved a heterogenously dense breast that contained an invasive, poorly differentiated, ductal adenocarcinoma of approximately 25×30 mm in size. The presence of the cancer mass and its size were diagnosed by mammography and conventional B-mode ultrasound. The ultrasound examination showed an irregularly shaped hypoechoic mass with spiculations and associated shadowing. The breast was encircled by the toroidal array in a similar fashion to the phantom experiments and the temperature of the water bath was 22.4°C.

III. RESULTS

This section presents the reconstructions obtained by applying the imaging methods introduced in Sec. II to the ultrasound measurements performed with the prototype scanner for the phantom and the human breast.

10

A. Phantom study

1. CW images

Figure 4(a) is the sound-speed map of a slice of the phantom obtained with CW TDT at 750 kHz. The image shows the presence and shape of the four inclusions and the skin of the phantom. These characteristics match well with those observed on the X-ray CT image in Fig. 3(b). A careful analysis of Fig. 4(a) also reveals the presence of the irregular contour of the glandular region. However, this is masked by the appearance of the first grating lobe caused by the large diameter of the phantom (the phantom diameter is 40 mm larger than the maximum object diameter of 80 mm at λ=2 mm). The artifact observed between the four inclusions is located at the center of the array and is due to incoherent random noise as shown in the next subsection.

Figure 4(b) is the CW RDT image at 750kHz. The image is noisy and none of the structures of the phantom can be observed. This is the combined effect of weak backscattering and speckle noise.

Figure 4(c) is the CW RI at 750kHz. As in the case of Fig. 4(b), the image is noisy; however, the outline of the phantom is now more clearly visible. This enhancement over RDT can be explained by observing that RI amplifies the spatial frequencies closer to $2k$, thus improving the reconstruction of boundaries of sudden impedance contrast such as the phantom skin.

2. WB images

WB images are obtained by coherent superposition of monochromatic reconstructions in the frequency range between 700 and 800 kHz. Note that for the scanner used in this experiments, the lower limit is dictated by the bandwidth of the transducers that have a low output power below 700kHz, whereas the upper limit is chosen to limit the effects of spatial aliasing since λ decreases as the frequency increases.

Figures 4(d),(e),(f) are the WB versions of the corresponding CW images in Figs. 4(a), (b), and (c). Comparison of Figs. 4(a) and 4(d) shows that WB TDT leads to the suppression of the central artifact, implying that it is caused by random incoherent noise. Moreover, the contrast of the masses relative to the glandular region improves as well as the definition

11

of the glandular region outline. Overall, the reconstruction in Fig. 4(d) exhibits striking similarities with the characteristics observed in the X-ray CT image in Fig. 3(b) despite the fact that X-ray CT provides a density map.

The WB RDT image in Fig. 4(e) shows an improvement over the CW RDT of Fig. 4(b); the contour of the glandular region, the skin and two of the inclusions are now visible. However, the estimation of the sound speed is incorrect. An even greater enhancement is observed for the RI in Fig. 4(f) that improves the reconstruction of the glandular region outline and the skin, and shows the second tumor.

3. Coherent versus incoherent imaging

Figure 5(a) shows a WB RI over the frequency range between 700 to 800 kHz obtained by the incoherent superposition described by eq. (10). As pointed out in Sec. II C, incoherent superposition attenuates the speckle contrast, and indeed Fig. 5(a) has a lower contrast than the image obtained with coherent superposition Fig. 5(b). However, only the reconstruction of the skin of the phantom is improved whereas, the image of the interior deteriorates. Moreover, the incoherent superposition does not lead to the reduction of incoherent noise and results in a magnification of the artifact at the center of the array.

4. TDT versus CUT

Figure 6(a) is the CUT sound-speed map of the same slice of the phantom imaged with TDT [Fig. 6(b)]. Despite the fact that CUT is using the full bandwith of the signal that is centered at 1.3 MHz and the wavelength is approximately one half of the wavelength used in the TDT reconstruction, the TDT image has superior resolution, providing sharper edges for the masses and more accurate sizing.

On the other hand, the contour of the glandular region is more clearly visible in the CUT image. This is due to the fact that the aliasing phenomenon that causes the grating lobe in TDT is not present in the CUT image. In fact, under the ray approximation the spacing between the sensors of the array has to be not larger than the smallest scattering feature in the object to avoid streak artifacts[16] in CUT. This condition is met by the toroidal array for which the ultrasound element spacing is 2.5 mm.

B. *In Vivo* study

Figure 7 is equivalent to Fig. 4 and refers to a coronal slice of the breast. The images lead to the same observations about CW and WB imaging for the breast phantom; therefore, these will not be repeated here. Instead, attention is paid to the structures contained in the images of Fig. 7. In particular, Figs. 7(a) and (d) (the CW and WB TDT images) show the skin of the breast and an entangled network of structures close to the center of the slice. It should be noticed that the breast is larger than the phantom and therefore, the image artifacts due to the grating lobe are enhanced as confirmed by the blurred reconstruction of the portion of the skin at the top of Figs. 7(a) and (d).

The arrows in Fig. 7 point at a region that contains the cancerous mass of approximately 20 mm in size. With reference to Fig. 7(d) it is possible to observe a number of structures departing from the lower part of the mass and penetrating into the surrounding glandular tissue. These same structures result in irregular features along the boundary of the mass that resemble the speculations observed in B-mode ultrasound images of certain types of malignant tumors.

The mass can also be seen to have an effect on the WB RDT image in Fig. 7(e) where it appears as a hypoechoic lesion. The same image also shows a number of fibrous structures in the lower-right quadrant, close to the skin. These structures are also found in the transmission image, Fig. 7(d), and the RI image, Fig. 7(f).

Figure 8 shows a comparison of the CUT reconstruction of the breast with the TDT image as in Fig. 6 for the phantom. However, while in the case of the phantom it is possible to observe a good correlation between the two sound-speed maps, in the *in vivo* case the same correlation cannot be found. Indeed, the CUT image indicates the presence of a region of high speed of sound at the location of the cancer mass [pointed by the harrow in Fig. 8(a)] whereas the TDT image dose not provide a significant deviation from the sound speed in the glandular region. Moreover, the CUT image shows a number of radial structures that depart from the cancer mass. These appear to radiate at approximately regular angular intervals and remind of the streak artifacts observed in CT images[16].

IV. DISCUSSION

The comparison of the phantom reconstructions obtained with CUT and TDT [Fig. 6] confirms that TDT provides higher resolution than CUT, leading to a more reliable detection and accurate sizing of the phantom inclusions. This demonstrates the importance of diffraction effects in ultrasound tomography. However, when the same comparison is carried out for the *in vivo* data set, CUT indicates the presence of a region of high sound speed at the location of the cancer mass, but that is not observed in the TDT image. The reason for this difference is not clear yet and is the subject of an ongoing investigation.

The network of fine structures observed at the center of the TDT image, which are not visible in the CUT image, could correspond to the milk ducts and Cooper's ligaments. In particular, the fibrous structures visible in the lower-right quadrant of Fig. 8(b), in the subcutaneous fat layer close to the skin, could be cross-sections of the Cooper's ligaments. The same structures can also be found in the WB RDT image, Fig. 7(e), and the WB RI image, Fig. 7(f). However, further *in vivo* tests followed by histology of biopsy samples need to be performed to confirm the validity of these hypotheses.

Both the phantom and *in vivo* results confirm that reflection imaging methods complement CUT by providing higher resolution reconstructions of the boundaries of sudden impedance variations. However, this is not true when comparing the reflection images with TDT that exhibits superior image resolution.

Reflection images are much noisier than transmission images. There are two reasons for this. First, the backscattered energy is lower than the transmitted one. As a result, the signal to random incoherent noise ratio is lower in reflection than in transmission. Second, reflection images are based on speckle noise contrast. Speckle is present in reflection images because the scattering produced by the fine structure of the object contribute to the backscattering measured along the aperture. On the other hand, the forward scattering associated with the same structures is encoded in the ballistic transmission that is deflected away from the object and does not reach the detectors, according to the physical argument proposed in Ref.[17]. As a result, transmission measurements are not affected by speckle noise.

Since backscattering measurements are mostly affected by incoherent random noise, WB coherent imaging leads to a greater image noise suppression in reflection than transmission. WB imaging [as described by the functional in eq. (11)], can lead to reduction of incoherent

14

random noise (not speckle noise) thanks to the averaging effect resulting from the coherent superposition of multiple monochromatic reconstructions. As a result, a wider bandwidth than that used in this paper is desirable, because the larger the bandwidth, the larger the ensemble of frequencies over which the averaging occurs. However, as noted in Fig. 5, this does not attenuate speckle noise that can only be reduced by incoherent superposition at the expenses of image signal to incoherent noise ratio.

Finally, the small fat sphere ($\sim$4 mm diameter) in the breast phantom is not detectable in any of the reflection images as it is masked by speckle noise, whereas it can be clearly observed in the transmission images, indicating that, for the array configuration considered in this paper, transmission measurements are more sensitive to small masses than backscattering measurements. However, it should be stressed that the results shown in this paper refer to a relatively low frequency range (700-800kHz). As a result, the delectability of small lesions with reflection imaging could be improved by increasing the frequency.

V. CONCLUSIONS

This paper has investigated the role of diffraction and coherence in breast ultrasound tomography. It has been shown that diffraction effects can be used in transmission diffraction tomography (TDT) to improve image resolution over computerized ultrasound tomography (CUT) that is based on the ray approximation of geometrical optics. For the first time it has been shown that TDT can be used for cancer detection *in vivo*. Moreover, the *in vivo* study suggests that TDT may be able to image very complex structures inside the breast such ducts and Cooper's ligaments.

While reflection imaging methods complement the information in CUT images, they do not reveal any additional characteristics that are not present in the TDT image. Indeed, TDT could image a 4 mm inclusion in the phantom that was not visible in the reflection images.

Finally, coherent superposition of continuous wave (CW) images obtained at different frequencies is beneficial to reflection imaging because it reduces the effects of incoherent random noise. The same improvement is not observed in TDT since the signal-to-noise ratio is higher in transmission than in reflection. Therefore, since narrowband transducers have a better response than wideband ones, it can be concluded that narrowband insonification

is optimal for TDT.

Acknowledgments

[1] J. F. Greenleaf, S. A. Johnson, S. L. Lee, G. T. Herman, and E. H. Wood, "Algebraic reconstruction of spatial distributions of acoustic absorption within tissue from their two-dimensional acoustic projections," in P. S. Green, editor, *Acoustical Holography* (Plenum Press, New York, 1973), vol. 5, 591–603.

[2] J. F. Greenleaf, S. A. Johnson, W. F. Samayoa, and F. A. Duck, "Algebraic reconstruction of spatial distributions of acoustic velocities in tissue from their time-of-flight profiles," in P. S. Green, editor, *Acoustical Holography* (Plenum Press, New York, 1975), vol. 6, 71–90.

[3] P. L. Carson, C. R. Meyer, A. L. Scherzinger, and T. V. Oughton, "Breast imaging in coronal planes with simultaneous pulse echo and transmission ultrasound," Science **214**, 1141–1143 (1981).

[4] T. M. Kolb, J. Lichy, and J. H. Newhouse, "Comparison of the performance of screening mammography, physical examination, and breast US and evaluation of factors that influence them: An analysis of 27,825 patient eveluation," Radiology **225**, 165–175 (2002).

[5] D. T. Ramsay, J. C. Kent, R. A. Hartmann, and P. E. Hartmann, "Anatomy of the lactating human breast redefined with ultrasound imaging," J. Anat. **206**, 525–534 (2005).

[6] A. P. Cooper, *On the anatomy of the breast* (Longman, Orme, Green, Brown and Longmans, London, 1840).

[7] J. G. Abbott and F. L. Thurstone, "Acoustic speckle: theory and experimental analysis," Ultrason. Imag. **1**, 303–324 (1979).

[8] J. H. Page, H. P. Schriemer, A. E. Bailey, and W. D. A., "Experimental test of the diffusion approximation for multiply scattered sound," Phys. Rev. E **52**, 3106–3114 (1995).

[9] R. L. Weaver and O. L. Lobkis, "Diffuse fields in ultrasonics and seismology," Geophysics **71**, S15–S19 (2006).

[10] M. P. Andre, M. P. Janee, H. S., G. P. Otto, B. A. Spivey, and P. D. A., "High-speed data acquisition in a diffraction tomography system employing large-scale toroidal arrays," Int. J. Imag. Syst. Tech. **8**, 137–147 (1997).

[11] F. Lin, A. I. Nachman, and R. C. Waag, "Quantitative imaging using a time-domain eigenfunction method," J. Acoust. Soc. Am. **108**, 899–912 (2000).

[12] R. C. Waag, F. Lin, T. K. Varslot, and J. P. Astheimer, "An eigenfunction method for re-

construction of large-scale and high-contrast objects," IEEE Trans. Ultrason. Ferroelectr. Freq. Control **54**, 1316–1332 (2007).

[13] N. Duric, L. Littrup, P. Poulo, A. Babkin, R. Pevzner, E. Holsapple, O. Rama, and C. Glide, "Detection of breast cancer with ultrasound tomography: First results with the Computed Ultrasound Risk Evaluation (CURE) prototype," Med. Phys. **34**, 773–785 (2007).

[14] S. R. Deans, *The Radon transform and some of its applications* (Wiley, New York, 1983).

[15] P. R. Williamson and M. H. Worthington, "Resolution limits in ray tomography due to wave behavior: Numerical experiments," Geophysics **58**, 727–735 (1993).

[16] A. C. Kak and M. Slaney, *Principles of computerized tomographic reconstruction* (IEEE Press, New York, 1999).

[17] F. Simonetti, L. Huang, and N. Duric, "A multiscale approach for high-resolution ultrasound tomography of complex three-dimensional objects," submitted for publication (2007).

[18] M. Born and E. Wolf, *Principles of Optics* (Cambridge University Press, Cambridge, 1999).

[19] E. Wolf, "Three-dimensional structure determination of semi-transparent objects from holographic data," Opt. Commun. **1**, 153–156 (1969).

[20] F. Simonetti and Huang, "From beamforming to diffraction tomography," J. Appl. Phys. **103**, 103110 (2008).

[21] J. W. Goodman, *Speckle phenomena in optics* (Roberts and Company Publisher, Greenwood Village, USA, 2007).

[22] F. Simonetti, L. Huang, N. Duric, and O. Rama, "Imaging beyond the Born approximation: An experimental investigation with an ultrasonic ring array," Phys. Rev. E **76**, 036601 (2007).
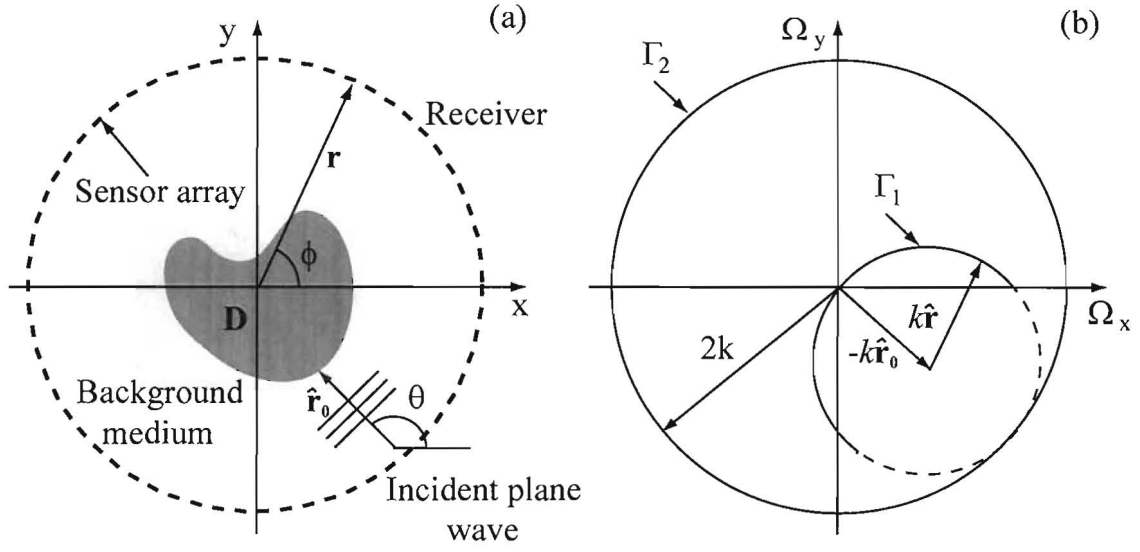
FIG. 1: (a) Diagram of a toroidal array used in ultrasound tomography. (b) Two dimensional K-space showing how the scattered field measured in the direction $\hat{\mathbf{r}}$ and due to an incident plane wave from direction $\hat{\mathbf{r}}_0$ maps onto the point $\Omega = 2\pi/\lambda(\hat{\mathbf{r}}_0 - \hat{\mathbf{r}})$ of the K-space.
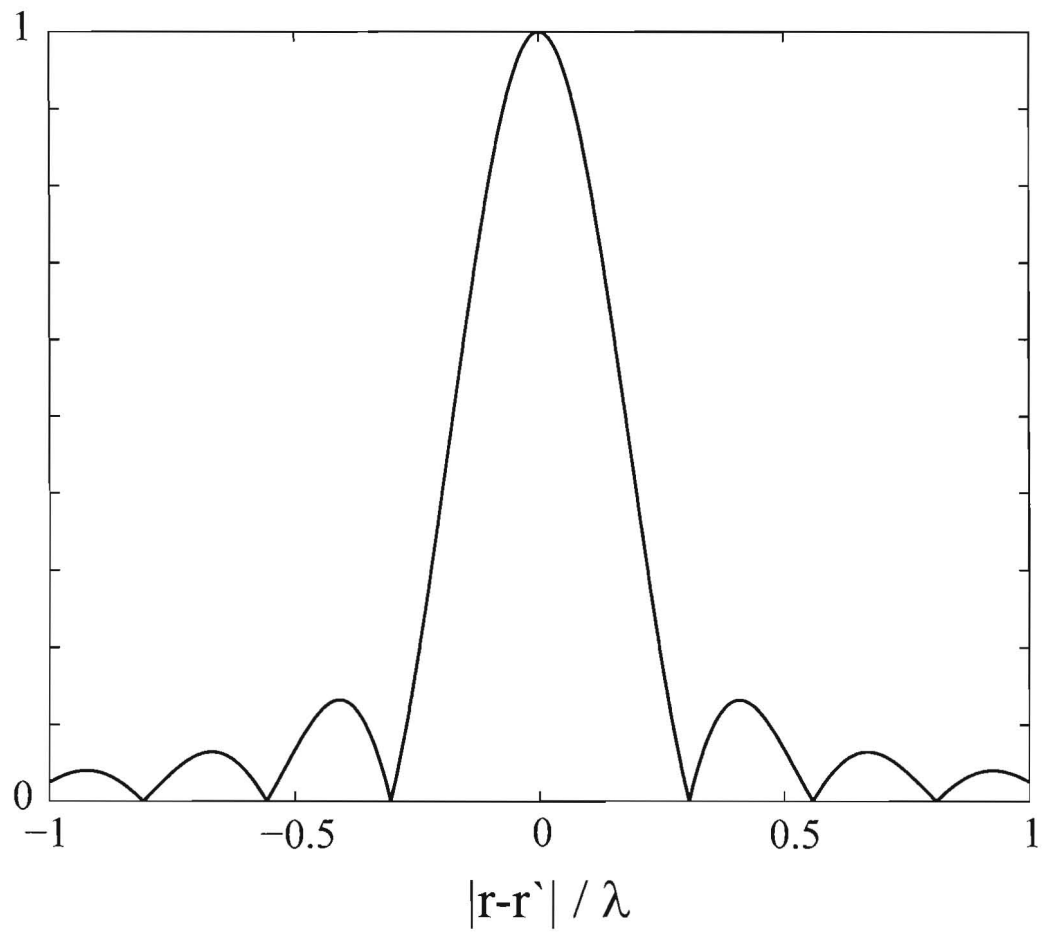
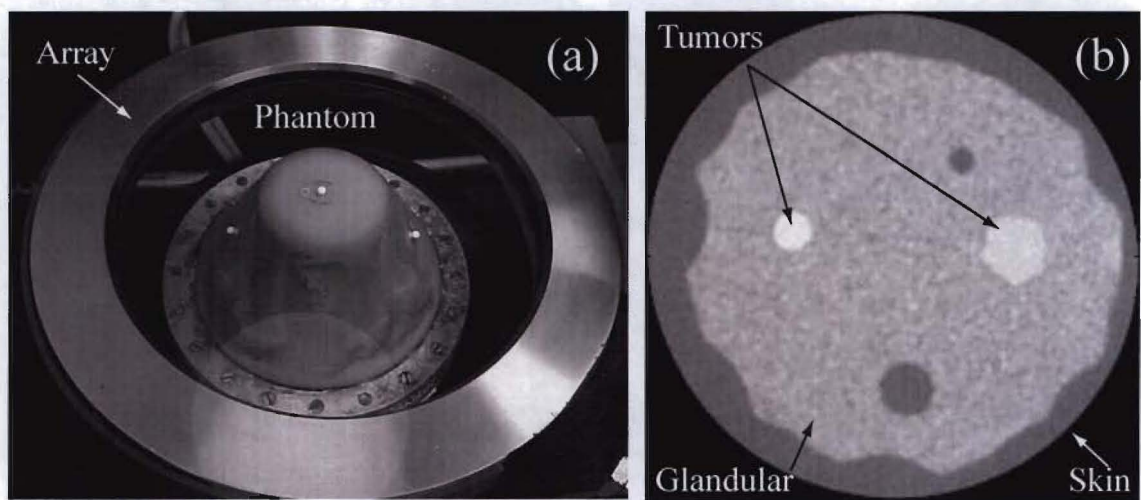FIG. 2: Normalized modulus of the point spread function for 2-D diffraction tomography.

FIG. 3: (a) Photograph showing the complex 3-D breast phantom, the toroidal array and their relative position; (b) X-ray CT of a coronal slice of the phantom showing the four inclusions, the glandular tissue and the skin.

FIG. 4: Coronal slice of the breast phantom reconstructed with different imaging methods: (a-b) CW images at 750kHz (d-f) WB images between 700 and 800kHz. (a), (d) Transmission diffraction tomography; (b), (e) Reflection diffraction tomography; (c), (f) Reflection imaging.
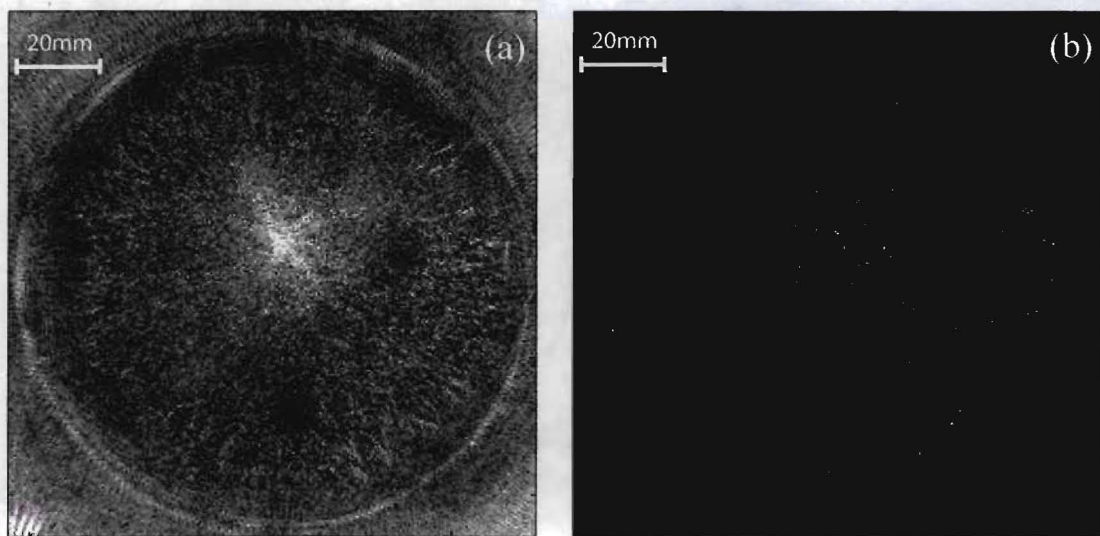
FIG. 5: Speckle suppression by incoherent superposition between 700 and 800kHz in a reflection image. (a) Incoherent image; (b) Coherent image, same as Fig. 4(f).
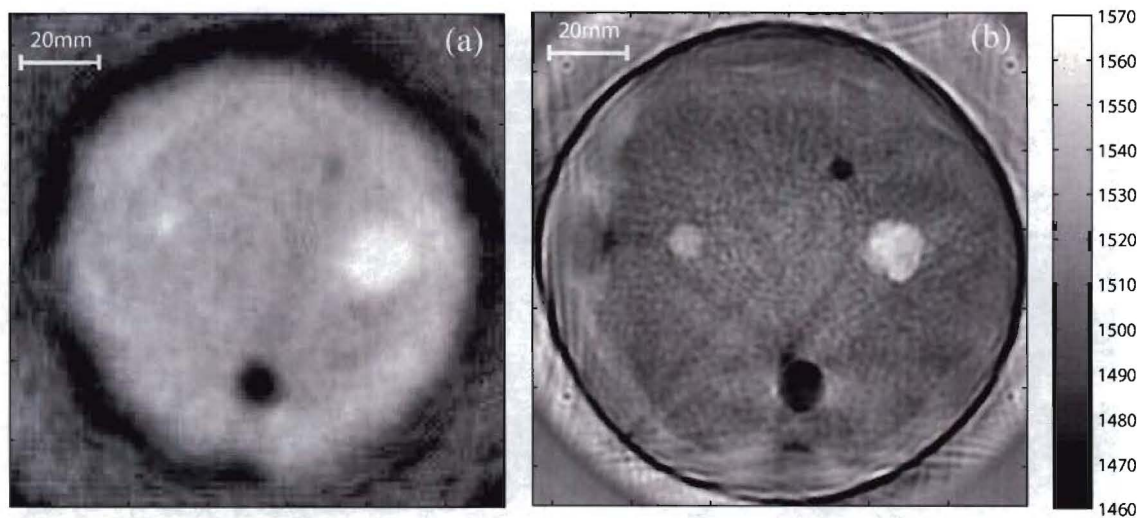
FIG. 6: Transmission tomography images of the phantom: (a) Computerized ultrasound tomography based on the ray approximation; (b) Transmission diffraction tomography, same as Fig. 4(d).
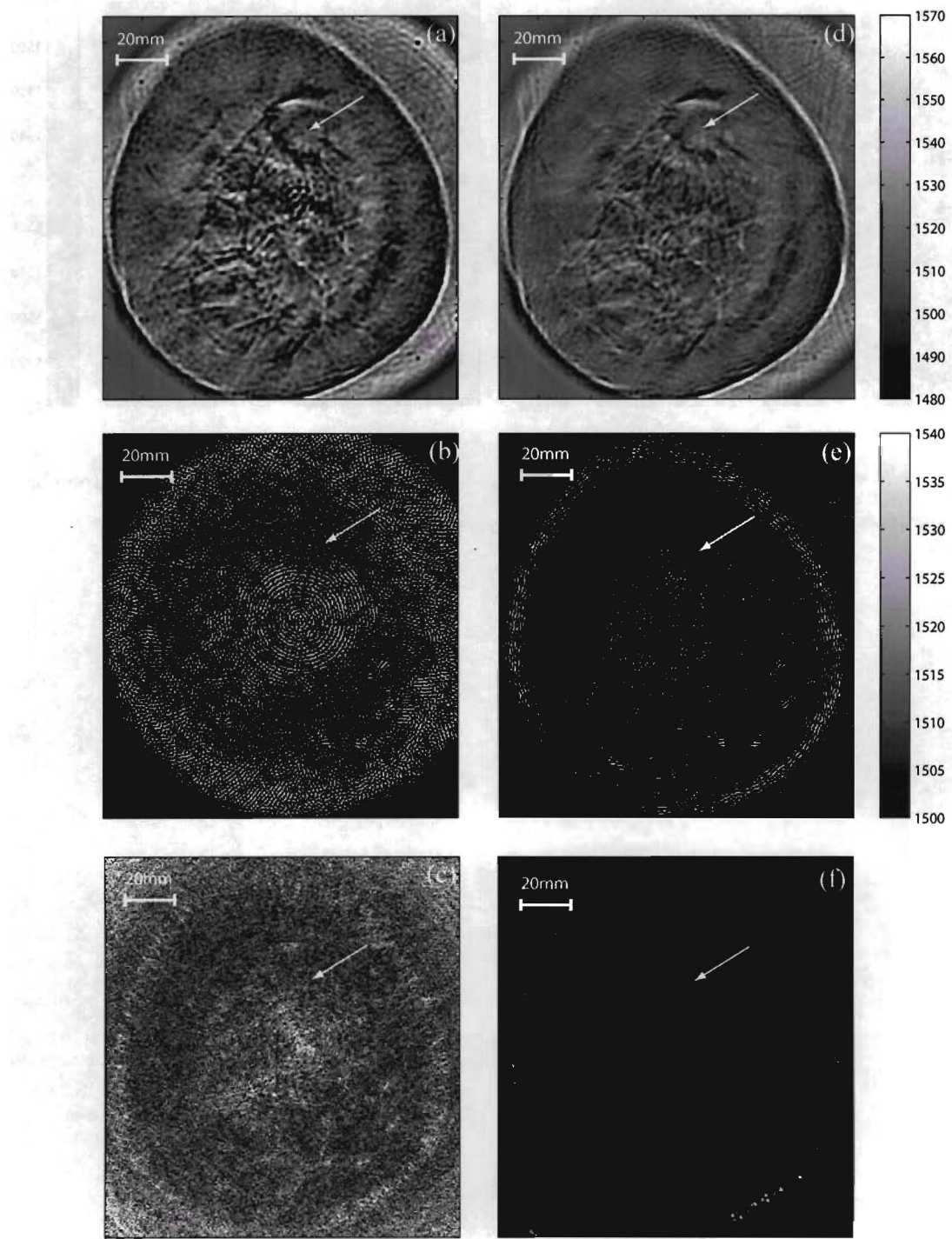
FIG. 7: Coronal slices of a human breast *in vivo* containing a cancerous mass pointed by the arrows: (a-b) CW images at 750kHz (d-f) WB images between 700 and 800kHz. (a), (d) Transmission diffraction tomography; (b), (e) Reflection diffraction tomography; (c), (f) Reflection imaging.
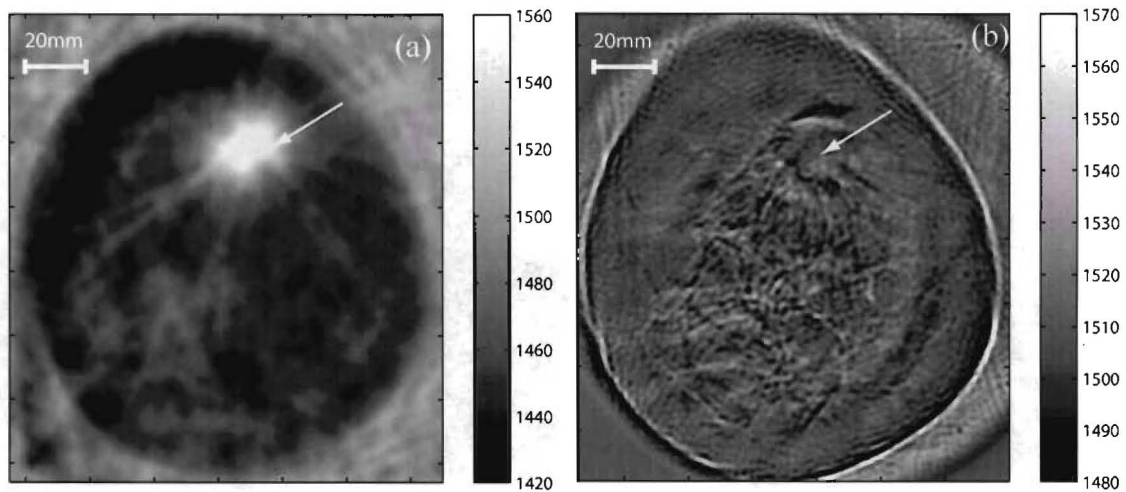
FIG. 8: *In vivo* transmission tomography images: (a) Computerized ultrasound tomography based on the ray approximation; (b) Transmission diffraction tomography, same as Fig. 7(d).